Combustion and Flame 195 (2018) 203–215

Contents lists available at ScienceDirect

Combustion and Flame

journal homepage: www.elsevier.com/locate/combustflame

A systematic approach to high-fidelity modeling and efficient simulation of supercritical fluid mixing and combustion

Xingjian Wang, Hongfa Huo, Umesh Unnikrishnan, Vigor Yang*

School of Aerospace Engineering, Georgia Institute of Technology, Atlanta, GA 30332, USA

ARTICLE INFO

Article history:
Received 8 November 2017
Revised 31 March 2018
Accepted 21 April 2018
Available online 17 May 2018

Keywords:
Supercritical fluid
SGS model of equation of state
Supercritical mixing and combustion
Dynamic adaptive chemistry
Correlated thermodynamics and transport
Tabulation

ABSTRACT

Advances in fluid-flow modeling and simulation techniques over the past two decades have improved understanding of the intricate flow physics and combustion dynamics in the supercritical regime. However, there remain many numerical issues to be addressed, including turbulence closure modeling, combustion modeling, and the evaluation of real-fluid thermodynamic and transport properties. The challenges can be broadly categorized into two areas: (1) achieving highly accurate simulation through inclusion of all the necessary physics and (2) developing a computationally efficient framework to achieve simulation results in a reasonable turnaround time. This paper investigates these challenges and presents a systematic approach to achieve high-fidelity and efficient simulation of supercritical fluid mixing and combustion using large-eddy simulation (LES) techniques. The unresolved subgrid-scale (SGS) term in the filtered equation of state (EOS), which is generally neglected for ideal gases, becomes significant for real fluids, especially in regions of strong property gradients at supercritical conditions. The relative error for the filtered density can reach up to 40%, and this uncertainty can propagate and contaminate calculations of the conservation equations. Two closure models for the SGS term in the EOS are proposed: a gradient-based and a mixing-based approach. Both approaches reduce the modeling error considerably. Flamelet-based combustion models are also examined at supercritical conditions. The probability density functions (PDFs) for mixture fraction and scalar dissipation rate are evaluated using a data-driven approach. The presumed beta-function distribution accurately describes the PDF of the mixture fraction at low mixture fraction variance, but deviates at high variance (>0.01). The lognormal distribution can capture the shape of the extracted PDF of the scalar dissipation rate but underestimates the peak value. An alternative combustion model using finite-rate chemistry integrated with dynamic adaptive chemistry and correlated transport is developed, rendering a computationally efficient and affordable framework. The efficiency of evaluating real-fluid thermodynamic and transport properties, a computationally expensive procedure, is dramatically enhanced using tabulation and correlated dynamic evaluation techniques. Finally, suggestions are provided regarding opportunities for future research.

1. Introduction

Supercritical mixing and combustion have received significant attention over the past two decades, mainly because of increasing demand for higher thermal efficiency in propulsion and power-generation systems. The operating pressures in these systems often exceed the thermodynamic critical points of the fluids involved. Liquids initially injected at a subcritical temperature may heat up and experience a thermodynamic phase transition into the supercritical regime. Many distinctive behaviors occur during the transition and differ from the phenomena encountered at subcritical conditions, such as diminishing of surface tension and absence of droplet formation and a two-phase interface. As a result, single-phase-like, diffusion-dominated mixing takes place between dense and light fluids in the presence of large property gradients [1–4].

Extensive experimental studies have led to improved qualitative understanding of the fundamental physics involved in supercritical fluid flows [5–13]. However, such measurements are limited by the extreme operating conditions and by the currently available experimental techniques. Computational techniques serve as a powerful tool to provide more detailed information about the flow structures and dynamics at supercritical conditions, and many numerical modeling and simulation studies have been carried out in this area. Computational modeling, however, poses a variety of challenges, including the classical closure issues associated with turbulent combustion and a unique set of problems introduced by thermodynamic non-idealities and transport anomalies [1]. Several

* Corresponding author.
E-mail address: vigor.yang@aerospace.gatech.edu (V. Yang).

https://doi.org/10.1016/j.combustflame.2018.04.030
0010-2180/

numerical solvers have been developed to tackle these challenges [14–21]. Collaborative efforts have also been made to assess the accuracy of different research codes using canonical subscale rocket combustors, such as the gaseous O_2 (GOX) /gaseous H_2 test rig [22] and the GOX/gaseous CH_4 test rig [23]. Similar predictions by different numerical solvers have been examined using a two-dimensional mixing layer configuration [24].

An important challenge for numerical solvers is the ability to achieve accuracy and stability in regions of steep gradients, which are manifested by sharp variations of thermodynamic and transport properties across the pseudo-boiling line, also known as the Widom line [25]. In this region, directly solving the full conservation equations of mass, momentum, species, and energy in a coupled manner can cause erroneous pressure fluctuations because of insufficient grid resolution [26]. Wang et al. [27] defined a fluid transition layer where the density gradient exceeds the 90% of its maximum value. The transition layer connects the compressed liquid regime to the supercritical regime, and it must be carefully treated to resolve the property gradients and prevent abnormal fluctuations of these variables. To mitigate spurious pressure oscillations, Terashima and Koshi [28] introduced a pressure evolution equation to replace the energy conservation equation and solved pressure along with other independent variables simultaneously. Ma et al. [20] applied an extended double-flux method to transcritical flows to overcome the same issue. These methods, however, cannot ensure energy conservation. Another approach is dual time-stepping integration with a preconditioning scheme [29,30], in which pressure is considered as one of the primitive variables and solved in every pseudo-time iteration. The pseudo-time convergence gives the pressure without unphysical oscillations, and it substitutes back to the original conservation equations to obtain a time-accurate solution. This methodology is implemented in the studies described here.

Turbulence closure remains a challenge for modeling supercritical flows. Although direct numerical simulations (DNS) resolve all the turbulent scales and steep gradients of fluid properties, they are constrained to simple flows with low Reynolds numbers and low density ratios [15,31–35]. DNS is computationally prohibitive for problems with practical configurations, which include complex geometries and high Reynolds numbers. The large-eddy-simulation (LES) technique has been widely employed to simulate operational systems at elevated pressures [19,36–42]. In LES, the unclosed subgrid scale (SGS) terms must be carefully modeled. In most studies, however, the SGS models developed for low-pressure turbulent flows have been directly applied to supercritical regimes without appropriate justification. The traditional Smagorinsky model leads to unsatisfactory results in the transcritical and supercritical regimes [43]. Furthermore, flow properties, such as compressibility factor and specific heat, are generally calculated from the LES-resolved variables, without considering the effect of the corresponding SGS fluctuations. These SGS terms, which are negligible at low pressures may become significant and even comparable to the leading-order terms (such as the convection terms) at high pressures [33,43,44]. In particular, the SGS term in the filtered equation of state (EOS) plays an essential role in obtaining filtered pressure (or density) accurately [45]. Proper modeling of the SGS term in the filtered EOS at supercritical pressures is one of the focal points in the current study of supercritical fluid flows and combustion.

Modeling turbulence/chemistry interactions (TCI) is another challenging task. For non-premixed systems, chemical reactions can only take place when fuel and oxidizer are mixed at a molecular level. Molecular mixing of scalar quantities and subsequent chemical reactions in turbulent flows occur at the smallest scales and are characterized by the scalar dissipation rate. This implies that chemical source terms typically cannot be resolved in LES and must be modeled. There are a variety of turbulent-combustion models available, such as flamelet-based models [46–49], the conditional moment closure model (CMC) [50], the eddy-dissipation-concept (EDC) model [51], the thickened-flame model [52], the linear-eddy mixing (LEM) model [53], and the transported probability density function (TPDF) [54], among others. The advantages and challenges of these models have recently been reviewed for aero-propulsion applications [55,56] and high-speed propulsion systems [57]. In most of these models, the probability density function (PDF) plays a crucial role. For conserved scalar models, a beta-function distribution is pressumed for the marginal filter PDF of the mixture fraction. Its validity has been successfully assessed against experimental and DNS data for various flows at low pressures [58,59]. However, it has been directly applied to high-pressure simulations [42,45,60], without validation. The applicability of the beta-function PDF for the filtered mixture fraction in supercritical flows is examined in the present work. On the other hand, the finite chemistry model does not make inherent assumptions about the PDF of flow quantities, and instead directly solves the chemical kinetics based on the instantaneous thermodynamic state of the mixture. The challenge is to model the subgrid turbulence-chemistry interactions, given the prohibitively large computational cost associated with detailed chemistry mechanisms.

Supercritical flows typically include dense fluids with high Reynolds (Re) numbers, and hence cover a broad range of turbulent length and time scales. In the transcritical flow regime for a typical rocket combustor, the density ratio can be as high as 100, and the transition region is on the order of 10 μm. Extremely fine grid distribution is required to resolve the density stratification. This in turn dramatically increases the computational cost. The situation becomes even more severe when real-fluid property evaluation is involved. The time required for the computation of thermodynamic and transport properties can be about 50% of the total CPU time. To alleviate the situation, acceleration techniques such as GPU acceleration [61] and tabulation [62,63], have been explored. Two techniques, a tabulation-based method and a correlated dynamic evaluation method, are explored in the present work for time-efficient real-fluid property evaluation.

The purpose of this paper is to report the authors' efforts to systematically investigate and address the key modeling and simulation challenges associated with supercritical fluid mixing and combustion. Several important aspects, including SGS closure, turbulence/chemistry interactions, and real-fluid property evaluation, are discussed. The rest of the paper is organized as follows: Section 2 presents the theoretical framework, and Section 3 demonstrates the state-of-the-art simulations using this framework. Section 4 then discusses the details of issues and strategies for high-fidelity modeling and efficient simulation, in terms of developing SGS models for EOS, examining combustion models, and accelerating evaluation of real-fluid thermodynamics and transport properties. Finally, key conclusions of the work and future directions are summarized in Section 5.

2. Theoretical framework

2.1. Conservation equations

The underlying physiochemical processes of supercritical combustion involve real-fluid behaviors, multi-species transport, chemical reactions, and turbulent mixing, as well as turbulence/chemistry interactions over a wide range of time and length scales. The governing equations for modeling such intricate phenomena must be addressed carefully. In this section, the full conservation equations of mass, momentum, energy, and conserved scalars are first presented, and then the Favre-filtered conservation

equations and unclosed SGS terms are introduced. The conservative form of the equations is written as follows,

Mass:

$$\frac{\partial \rho}{\partial t} + \frac{\partial \left(\rho u_j\right)}{\partial x_j} = 0 \tag{1}$$

Momentum:

$$\frac{\partial (\rho u_i)}{\partial t} + \frac{\partial \left(\rho u_i u_j + p\delta_{ij}\right)}{\partial x_j} = \frac{\partial \tau_{ij}}{\partial x_j} \tag{2}$$

Energy:

$$\frac{\partial (\rho e_t)}{\partial t} + \frac{\partial \left((\rho e_t + p) u_j\right)}{\partial x_j} = \frac{\partial}{\partial x_j}\left(u_i \tau_{ij} + q_j\right) \tag{3}$$

Species:

$$\frac{\partial (\rho Y_k)}{\partial t} + \frac{\partial \left(\rho u_j Y_k\right)}{\partial x_j} = \frac{\partial}{\partial x_j}\left(\rho D_k \frac{\partial Y_k}{\partial x_j}\right) + \dot{\omega}_k \tag{4}$$

where $\rho, u,$ and p represent density, velocity, and pressure, respectively. e_t is the total energy per unit mass, $e_t = e + u_i u_i/2$, and e is the specific internal energy. i and j denote spatial coordinate indices. τ_{ij} and q_j are the viscous stress tensor and heat flux, respectively. Body forces, radiation, and Soret and Dufour effects are neglected. Note that in the energy equation the heat release from chemical reactions is embedded in the specific enthalpy, which consists of the sensible enthalpy and the enthalpy of formation.

An EOS is needed to describe the fluid volumetric properties $p - \rho - T$ and complement Eqs. (1)–(4) for a well-posed system. Several cubic EOSs are available for real fluids [64]. In the current study, a modified Soave–Redlich–Kwong (SRK) EOS [65] is employed, because of its validity over a broad range of fluid states, and its easy implementation, as follows:

$$p = \frac{\rho R_u T}{MW - b\rho} - \frac{a\alpha}{MW} \frac{\rho^2}{MW + b\rho} \tag{5}$$

Alternatively, Eq. (5) can be written in terms of the compressibility factor, Z:

$$p = Z\rho RT \tag{6}$$

where R is the specific gas constant ($R = R_u/MW$). For an ideal gas, $Z = 1$, Eq. (6) reverts to the ideal-gas EOS.

2.2. LES formulation

In LES, large-scale energy-containing and anisotropy motions are resolved, while small-scale motions that tend to be universal are modeled. Low-pass filtering is performed on Eqs. (1)–(4) to separate grid-resolved filtered terms from SGS terms. The filter function should theoretically accommodate small-scale fluctuations in both space and time [55]. The present study considers spatial filtering only by assuming that the truncation errors associated with the temporal SGS fluctuations are small. A box filter is selected as the filter function, among others [66]. With the application of the filtering operation, the governing equations for LES are obtained in the following format:

$$\frac{\partial \rho\left(\tilde{\mathbf{Q}}\right)}{\partial t} + \frac{\partial \bar{\rho}\tilde{u}_j}{\partial x_j} = \frac{\partial \rho^{sgs}}{\partial t} \tag{7}$$

$$\frac{\partial \rho\left(\tilde{\mathbf{Q}}\right)\tilde{u}_i}{\partial t} + \frac{\partial \left(\bar{\rho}\tilde{u}_i\tilde{u}_j + \bar{p}\delta_{ij}\right)}{\partial x_j} = \frac{\partial \left(\tau_{ij}\left(\tilde{\mathbf{Q}}\right)\right)}{\partial x_j} - \frac{\partial T_{ij}^{sgs}}{\partial x_j} - \frac{\partial \tau_{ij}^{sgs}}{\partial x_j} + \frac{\partial \left(\rho^{sgs}\tilde{u}_i\tilde{u}_j\right)}{\partial x_j} + \frac{\partial \left(\rho^{sgs}\tilde{u}_i\right)}{\partial t} \tag{8}$$

$$\frac{\partial \rho\left(\tilde{\mathbf{Q}}\right)e_t\left(\tilde{\mathbf{Q}}\right)}{\partial t} + \frac{\partial \left[\rho\left(\tilde{\mathbf{Q}}\right)e_t\left(\tilde{\mathbf{Q}}\right) + \bar{p}\right]\tilde{u}_j}{\partial x_j} = \frac{\partial [\tilde{u}_i\tau_{ij}\left(\tilde{\mathbf{Q}}\right) + \sigma_{ij}^{sgs} + q_j\left(\tilde{\mathbf{Q}}\right) - q_j^{sgs} - H_j^{sgs}]}{\partial x_j} + \frac{\partial (\rho e_t)^{sgs}}{\partial t} + \frac{\partial \left((\rho e_t)^{sgs}\tilde{u}_j\right)}{\partial x_j} \tag{9}$$

Here the commutation errors between filtering and spatial/temporal gradients are neglected. The traditional unclosed SGS terms include shear stresses (T_{ij}^{sgs}), viscous work (σ_{ij}^{sgs}), and energy flux (H_j^{sgs}). Many closure models have been proposed, such as the Smagorinsky model, dynamic models, the k-SGS model, and the scale-similarity model. The Smagorinsky model has been used for our LES-based framework.

As will be discussed in Section 2.5, the numerical scheme is a dual-time-stepping integration technique enforced with a preconditioning scheme. The physical variables, including density (ρ), shear stress tensor (τ_{ij}), specific total energy (e_t), and heat fluxes (q_j), are evaluated based on the primitive variable vector, $\mathbf{Q} = (p,\ u,\ v,\ w,\ T)^T$, that is, $\phi = \phi(\mathbf{Q})$. In most LES solvers, the filtered variable, $\widetilde{\phi(\mathbf{Q})}$, is often calculated as $\phi(\tilde{\mathbf{Q}})$ because the true $\mathbf{Q}$ is unknown. In other words, the contribution of the SGS fluctuations of the primitive variables ($\mathbf{Q}'' = \mathbf{Q} - \tilde{\mathbf{Q}}$) is not considered when filtering ϕ.

The neglect of the SGS fluctuations has not, however, been justified and it may, in fact, induce significant errors in calculating the filtered variables. Here we denote the difference between $\widetilde{\phi(\mathbf{Q})}$ and $\phi(\tilde{\mathbf{Q}})$ as SGS contributions in Eqs. (7)–(9), and they are defined as

$$\rho^{sgs} = \rho\left(\tilde{\mathbf{Q}}\right) - \bar{\rho} \tag{10}$$

$$\tau_{ij}^{sgs} = \tau_{ij}\left(\tilde{\mathbf{Q}}\right) - \bar{\tau}_{ij} \tag{11}$$

$$(\rho e_t)^{sgs} = \rho\left(\tilde{\mathbf{Q}}\right)e_t\left(\tilde{\mathbf{Q}}\right) - \bar{\rho}\widetilde{e_t} \tag{12}$$

$$q_j^{sgs} = q_j\left(\tilde{\mathbf{Q}}\right) - \bar{q}_j \tag{13}$$

Similarly, the filtered EOS becomes

$$\bar{p} = \bar{\rho}\tilde{Z}\tilde{R}\tilde{T} + p^{sgs}, \tag{14}$$

where $p^{sgs} = \bar{\rho}(\widetilde{ZRT} - \tilde{Z}\tilde{R}\tilde{T})$ takes into account the SGS fluctuations of the compressibility factor, temperature, and species components introduced during the filtering process.

In the present framework, pressure, instead of density, is treated as one component of the primitive-variable vector ($\mathbf{Q}$). Eq. (14) is used to solve the filtered density ($\bar{\rho}$) and can be rewritten as,

$$\bar{\rho} = \bar{p}/\ \tilde{Z}\tilde{R}\tilde{T} + \rho^{sgs}, \tag{15}$$

where $\rho^{sgs} = -p^{sgs}/\tilde{Z}\tilde{R}\tilde{T}$.

Most existing models neglect the contribution of this complex SGS term, and directly use the filtered primitive variables to calculate the filtered density (or pressure). This term, however, may become significant in many flow environments, where transcritical regimes occur, along with strong property gradients [45]. In the present work, two models for ρ^{sgs} are proposed, based on physics-based and data-driven approaches.

2.3. Turbulent combustion model

It is computationally prohibitive to solve the LES formulation for reacting flows with detailed chemical mechanisms and real-fluid properties. To alleviate this difficulty, the steady laminar

flamelet model (SLFM) [46] and flamelet/progress variable (FPV) model [48] have been used here. The basic assumption of the SLFM is that chemical timescales are so short that reactions occur in a thin layer around the stoichiometric mixture, on a scale smaller than the smallest turbulence scales. The steady-state assumption, however, becomes inaccurate when slow chemical processes, such as pollutant formation and flame extinction, take place. The FPV model is implemented with a progress variable to account for these unsteady events. In both models, calculations of chemical reactions are decoupled from the turbulent field, and hence can be performed before the simulation. In the SLFM, the mixture fraction (f) and scalar dissipation rate (χ) are used as input parameters; in the FPV model, a progress variable (C) replaces the scalar dissipation rate as the second input parameter. The transport equations for mixture fraction and progress variable are given as,

$$\frac{\partial \rho f}{\partial t}+\frac{\partial (\rho u_j f)}{\partial x_j}=\frac{\partial}{\partial x_j}\left(\rho D\frac{\partial f}{\partial x_j}\right) \tag{16}$$

$$\frac{\partial \rho C}{\partial t}+\frac{\partial (\rho u_j C)}{\partial x_j}=\frac{\partial}{\partial x_j}\left(\rho D\frac{\partial C}{\partial x_j}\right)+\dot{\omega}_C \tag{17}$$

The differential diffusion effect is neglected and uniform mass diffusivity is assumed for all species. The progress variable for hydrocarbon fuels is usually defined as the sum of the mass fractions of major products: $C=Y_{H2O}+Y_{CO2}+Y_{CO}+Y_{H2}$; the production rate of the progress variable is the sum of production rates of these species. These two transport equations replace the species equation Eq. (4)) and are solved as part of the governing equations. Following the procedures described in Section 2.2, Eqs. (16) and ((17) are filtered as,

$$\frac{\partial \rho(\tilde{\mathbf{Q}})\tilde{f}}{\partial t}+\frac{\partial \rho(\tilde{\mathbf{Q}})\tilde{u}_j\tilde{f}}{\partial x_j}=\frac{\partial}{\partial x_j}\left(\rho(\tilde{\mathbf{Q}})D(\tilde{\mathbf{Q}})\frac{\partial \tilde{f}}{\partial x_j}-\Phi_j^{sgs}+j_f^{sgs}\right)+\frac{\partial\left(\rho^{sgs}\tilde{u}_j\tilde{f}\right)}{\partial x_j}+\frac{\partial \rho^{sgs}\tilde{f}}{\partial t} \tag{18}$$

$$\frac{\partial \rho(\tilde{\mathbf{Q}})\tilde{C}}{\partial t}+\frac{\partial \rho(\tilde{\mathbf{Q}})\tilde{u}_j\tilde{C}}{\partial x_j}=\frac{\partial}{\partial x_j}\left(\rho(\tilde{\mathbf{Q}})D(\tilde{\mathbf{Q}})\frac{\partial \tilde{C}}{\partial x_j}-\Psi_j^{sgs}+j_C^{sgs}\right)+\overline{\dot{\omega}}_c+\frac{\partial\left(\rho^{sgs}\tilde{u}_j\tilde{C}\right)}{\partial x_j}+\frac{\partial \rho^{sgs}\tilde{C}}{\partial t} \tag{19}$$

where $\Phi_j^{sgs}$and $\Psi_j^{sgs}$are SGS scalar fluxes. Other SGS terms, including j_f^{sgs}, $\rho^{sgs}\tilde{f}$, j_C^{sgs}, and $\rho^{sgs}\tilde{C}$, result from the filtering process as described in Section 2.2.

For both models, species mass fractions are retrieved from a pre-calculated flamelet library. For the SLFM, the input parameters for the library are filtered mixture fraction, variance of mixture fraction, and scalar dissipation rate from the flowfield. The species mass fractions in the library are filtered using:

$$\tilde{Y}_i(x,t)=\int_0^1\int_0^\infty Y_i(f,\chi)P(\chi)P(f)d\chi\,df \tag{20}$$

Beta-function distribution is assumed for the filter PDF of the mixture fraction, while lognormal distribution is applied for the filter PDF of the scalar dissipation rate. They are assumed to be statistically independent. The variance of the mixture fraction, $\widetilde{f''^2}$, is modeled as $K_b\bar{\rho}\overline{(\tilde{f}-\tilde{\bar{f}})^2}/\bar{\rho}$, using the scale similarity assumption [67]. For the FPV model, the scalar dissipation rate is replaced by the progress variable with a Dirac delta function distribution. The filtered reaction rate of the progress variable in Eq. (17) is obtained in a similar fashion:

$$\overline{\dot{\omega}}_c=\int_0^1\int_0^1\dot{\omega}_c(f,C)P(f)\delta(C-\tilde{C})dC\,df \tag{21}$$

In addition to the flamelet-based models, an efficient combustion model with finite-rate chemistry is developed and implemented as an alternative modeling strategy. The approach combines dynamic adaptive chemistry (DAC) and correlated transport (CoTran) to allow the treatment of finite-rate chemistry within the LES framework in a computationally affordable manner. DAC generates locally-optimized reduced kinetics for each spatial location and time step, and only reaction rates of active species and reactions are calculated. The kinetics reduction using path flux analysis starts from a user-defined list of preselected species (usually fuel and oxidizer), and calculates the correlation coefficients between the remaining species and selected species [68]. If the correlation coefficient of the remaining species is larger than a user-defined threshold, these species are added to the list of selected species. When no more species can be added, the reduced kinetics is generated.

A spatiotemporal correlation is further introduced to minimize the triggering of the local mechanism reduction. CoTran uses a similar correlation method to reduce the calculation of the mixture-averaged diffusion coefficients, including thermal conductivity, dynamic viscosity, and mass diffusivity. This framework has been successfully implemented on a canonical turbulent premixed flame [69], a temporally evolving turbulent non-premixed flame [70], and a turbulent partially premixed flame [71].

2.4. Property evaluation

Real-fluid property evaluation is important for modeling non-ideal thermodynamics and transport anomalies. According to fundamental thermodynamics theories, thermodynamic properties can be expressed as the summation of an ideal-gas counterpart and a departure function accounting for dense fluid corrections [1]. For example, Eqs. (22) and (23) list the expressions of specific internal energy and specific heat at constant pressure. The partial derivative terms in brackets are obtained using the SRK EOS given in Eq. (5). In the vicinity of the pseudo-boiling line (the transcritical regime), strong property gradients appear. Care must be taken to ensure numerical stability to avoid spurious property fluctuations. Transport properties are evaluated using the extended corresponding state principle. Detailed validation and implementation have been outlined in previous work [1,72].

$$e(T,\rho)=e_0(T)+\int_{\rho_0}^{\rho}\left[\frac{p}{\rho}-\frac{T}{\rho^2}\left(\frac{\partial p}{\partial T}\right)_\rho\right]_T d\rho \tag{22}$$

$$C_p(T,\rho)=C_{V_0}(T)-\int_{\rho_0}^{\rho}\left[\frac{T}{\rho^2}\left(\frac{\partial^2 p}{\partial T^2}\right)_\rho\right]_T d\rho+\frac{T}{\rho^2}\left(\frac{\partial p}{\partial T}\right)_\rho^2\Big/\left(\frac{\partial p}{\partial \rho}\right)_T \tag{23}$$

Real-fluid property evaluation is much more computationally expensive than ideal-gas calculations. Recent studies have shown that the computation time for the compressibility factor and thermodynamic and transport properties takes nearly 50% of the total CPU time for non-reacting flows [61,73]. The situation becomes more severe when chemical reactions and multiple species are involved. Nevertheless, the contributions of all constituent species to mixture properties must be taken into account. Two approaches, namely the tabulation and correlated dynamic evaluation techniques, are proposed to substantially improve the situation.

2.4.1. Tabulation

The physical properties can be pre-calculated and tabulated in a library, similar to a flamelet library. The property values for a given thermodynamic state can then be looked up through efficient data retrieval from the library, rather than evaluated at every iteration step. The property look-up table contains thermodynamic and transport properties of the mixture for a wide range of operating conditions. An important question is how to select the input parameters to build the correspondence between the flowfield and the library. Lacaze and Oefelein [62] conducted a sensitivity analysis of the flame structures to strain rate, pressure, and temperature in an opposed-jet configuration. They proposed the use of mixture fraction (f), pressure (p), and enthalpy (h) as input parameters. All other thermodynamic and transport properties, such as thermal conductivity, specific heat, and compressibility factor, were extracted from the library as a function of the input parameters.

In the present work, two input parameters, f and T are chosen, for two reasons. First, f and T are readily available from the LES solution. There is no need to calculate enthalpy 'on the fly.' Second, memory and computational overhead increase with the number of input parameters. It is always desirable to have a smaller look up table. Pressure fluctuation is generally very small compared to its mean value in the flowfield, and its effect on species components and subsequent property evaluation are minimal. For a non-reacting binary system, the mixture fraction essentially degenerates to the fuel mass fraction.

2.4.2. Correlated dynamic evaluation

Implementation of the method of correlated dynamic evaluation (CDE) is motivated by previous work [69,70] on developing an efficient transport model for ideal-gas finite-rate chemistry calculations. The approach is extended to both thermodynamic and transport properties in the current study. For a mixture, whether it is ideal-gas or real-fluid, the properties are spatiotemporally correlated. For example, a region far from the mixing layer or multi-species interaction region should have similar thermodynamic and transport properties. For a temporally evolving flow, the properties only vary slightly between adjacent time steps in some regions. Under these conditions, one-time property evaluation at one grid point is enough for each spatiotemporally correlated zone, and these calculated properties are passed to other grid points in the same zone and to other time steps whose properties are correlated. The key to this method is to select marker variables appropriately representing the characteristics of the thermophysical properties, and to carefully determine correlation criteria.

For thermodynamic properties, the state postulate indicates that only two independent intensive properties are needed to determine a thermodynamic state (a unique set of all thermodynamic properties) for a simple compressible substance. For a mixture of N species, the number of needed properties is $N+1$. A good selection of a group of marker variables is T, ρ (or p), and Y_k $(k = 1, \ldots, N-1)$. Then it is necessary to check whether this group can also suitably represent transport properties. It is known that dynamic viscosity, thermal conductivity, and mass diffusivity of a pure gas are a function of temperature at low pressures. The introduction of density accounts for real-fluid corrections. The transport properties of a mixture are calculated by a combination of mass-weighted values of individual species following the mixing rule. Therefore, the selected group (T, ρ and Y_k $(k = 1, \ldots, N-1)$) can be taken to sufficiently determine both thermodynamic and transport properties. The resulting correlation metric is established as follows,

$$corr = \left(\frac{\tilde{T} - \tilde{T}^0}{\tilde{T}^0}, \frac{\tilde{\rho} - \tilde{\rho}^0}{\tilde{\rho}^0}, \frac{\tilde{Y}_k - \tilde{Y}_k^0}{\tilde{Y}_k^0} \right); k = 1, \ldots, N-1 \qquad (24)$$

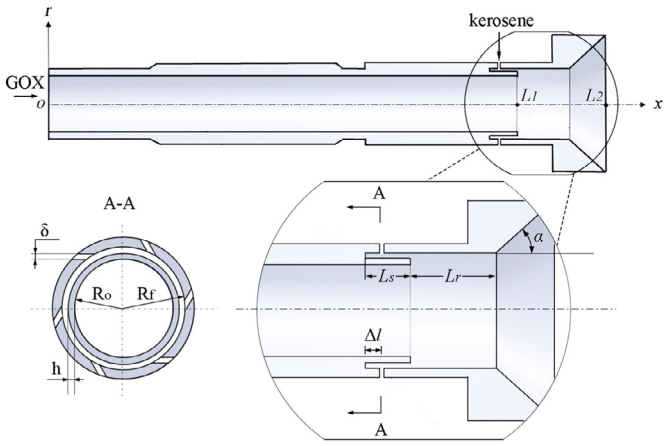

Fig. 1. Schematic of jet-swirl injector of RD-170 engine.

When $\|corr\|_\infty$ is smaller than a threshold value, ε, that is, when $\|corr\|_\infty \le \varepsilon$, the two states are treated as correlated in terms of properties. For a chemical system that consists of a vast number of species, it is impractical to include all species in the correlation metric; with a large number of species, the computational overhead for evaluating correlations increases enormously, and the performance of the approach is downgraded. Only major species are therefore included in the metric and minor species are ignored, since their contributions are negligible to the mixture properties. Note that some intermediate species and radicals are critical in chemical kinetics [69] and must be taken into account.

2.5. Numerical method

The numerical framework is based on a preconditioning scheme and a unified treatment of general-fluid thermodynamics [30,72]. It employs a density-based, finite-volume methodology, along with a dual-time-step integration technique [29]. Temporal discretization is achieved using a second-order backward difference, and the inner-loop pseudo-time term is integrated with a four-step Runge–Kutta scheme. Spatial discretization is obtained using a fourth-order central difference scheme in generalized coordinates. Fourth-order matrix dissipation, developed by Swanson and Turkel [74], is employed to ensure numerical stability and minimum contamination of the solution. Finally, a multi-block domain decomposition technique associated with the message passing interface technique is applied to optimize computation speed.

3. Capabilities of framework

The framework presented in Section 2 has been applied to simulate supercritical mixing and combustion in various configurations, including liquid droplets [75,76], laminar counterflows [77–79], shear coaxial injectors [16,37,42,80], and swirl injectors [27,41,81,82]. As a specific example, this section presents recent simulation results on the single-element injector used in the main combustion chamber of the RD170/180 engine, the most powerful liquid rocket engine to date, which was used for the Energia and Atlas V launch vehicles [83,84].

Figure 1 shows a schematic of the jet-swirl injector. GOX is injected axially into the center tube and liquid kerosene is introduced through six tangential orifices in the coaxial outer swirler. The operating pressure, 253 bar, greatly exceeds the critical values of oxygen (50.5 bar) and kerosene (21.7 bar). The inlet temperatures of GOX and kerosene are 687.7 K and 492.2 K, respectively. Kerosene undergoes a transcritical change of state from compressed liquid at injection to supercritical fluid in the flame

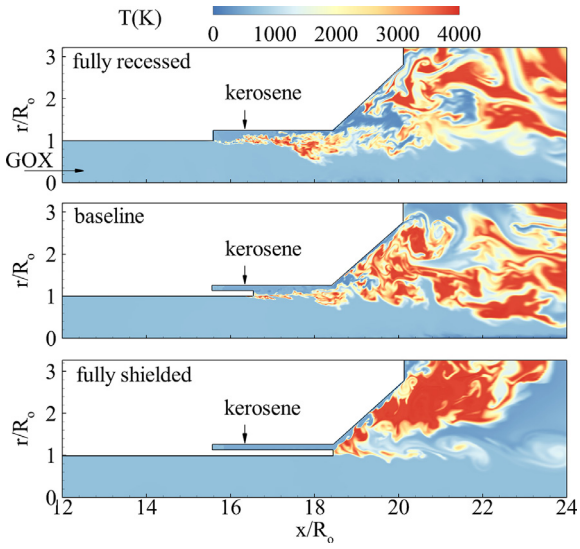

Fig. 2. Snapshot of the temperature field for different recess lengths.

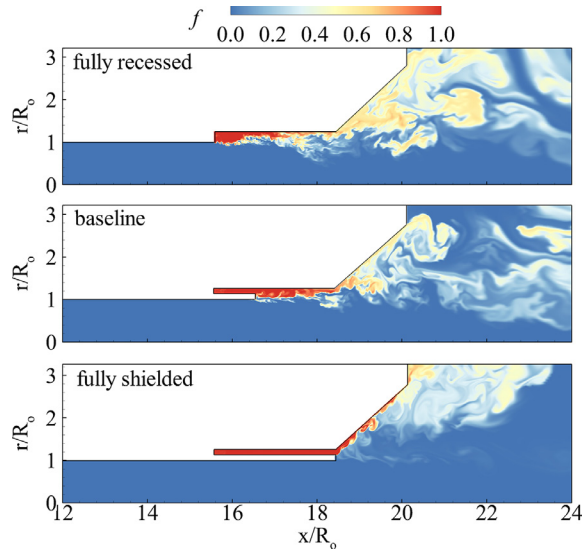

Fig. 3. Snapshot of the mixture fraction field for different recess lengths.

region, while GOX stays supercritical. The SLFM is used to model the TCI, because a priori study showed that the local strain rate in the current flowfield is much smaller than the extinction strain rate ($\sim 10^7$ s^{-1} at 253 bar) for oxygen/kerosene counterflow diffusion flames [79]. A skeletal chemical mechanism with 106 species and 382 reactions [85] is implemented for oxygen/kerosene combustion.

Figure 2 shows the instantaneous distributions of temperature near the injector exit for different recess lengths L_r. For all cases, the flame is anchored at the GOX post tip, and the anchoring point moves downstream with decreasing recess length. For the fully recessed (unshielded) case (L_r=16 mm), the thermal protection of the kerosene injection to the injector surface is removed and the kerosene flow pattern is like a jet in crossflow. This causes the shear layer to form at an earlier stage and significantly enhances the propellant mixing, producing a broader flame zone than in the baseline case (L_r=10.5 mm) at the injector exit.

For the fully shielded case (no recess, L_r=0), the flame ignites downstream of the injector. The swirl-induced centrifugal force drives the kerosene stream to flow along the taper surface, so that there is very limited mixing between GOX and kerosene. This can be clearly observed from the corresponding mixture fraction field in Fig. 3. In the fully shielded case, the fuel-rich mixture flows radially outward along the taper surface and the flame is restrained near the taper surface. The majority of the central GOX jet moves downstream without interaction with kerosene. As the recess length increases, the fuel entrainment improves and the mixing increases. The tradeoff is, however, a fuel-leaner mixture and higher temperature along the injector surface with increasing recess length. The high-temperature profile along the surface may endanger the hardware and/or intensify cooling requirements. In other words, the baseline case can provide a balance of efficient combustion and proper thermal protection.

The above results reveal the flame stabilization mechanism of the jet-swirl injector and offer guidance on the selection of recess length for injector optimization. The insights possible from such high-fidelity simulations would be extremely difficult (if not impossible) to achieve with experimental measurements or visualization techniques. Although these numerical simulations have improved our understanding of supercritical combustion in many ways, however, there remain a number of issues to be addressed. The rest of this paper will touch upon some of the critical issues raised in the introduction.

4. High-fidelity modeling and efficient simulation

4.1. SGS modeling

In this section, uncertainties of SGS models are examined using a previously-established two dimensional DNS database [44]. The physical model is a coaxial flow of liquid oxygen (LOX) and methane separated by a splitter plate with a shear layer formed in the downstream region. The thickness of the splitter plate is $\delta = 0.3$ mm. The inlet temperatures of LOX and methane are 120 K and 300 K, respectively. The ambient pressure is set to 100 bar and the momentum flux ratio of the LOX and methane streams is 1:2.7. The Reynolds number is about 1.5×10^5, based on the splitter plate thickness, the LOX/methane bulk velocity difference, and the LOX viscosity. The computational domain encompasses 20 mm axially and 10 mm radially downstream of the splitter plate. Because of the enormous computational cost of a three-dimensional simulation at such a high Reynolds number, a two-dimensional simulation was conducted. The total number of grid points is 1.2 million, with special refinement near the plate lip (501 grid points radially). This resolution has been validated in our previous study [44] to be sufficient to resolve and capture all the turbulent scales and property gradients in the flowfield.

Figure 4 shows the temperature and density distributions of the LOX/methane mixing and combustion. Unlike at subcritical pressure, where liquid atomization and droplet formation occur, here a thin shear layer forms between the LOX and methane and it behaves like single-phase mixing with finger-like structures. The density varies from a very high value of 1007 kg/m^3 on the LOX side to a small value of 74 kg/m^3 for the methane flow and 8 kg/m^3 for combustion products. The corresponding density ratios are 13.5 and 125, respectively. Variations of other thermodynamic properties show similar trends. The steepest property gradients appear within an extremely narrow region of approximately one-twentieth of the splitter plate thickness (15 μm), where 15 grid points are employed to resolve the gradients.

Generally, LES cannot capture these variations because of limited spatial resolution, as compared with DNS. Subgrid contributions to filtered properties must be carefully considered. Filtered thermodynamic properties ($\widetilde{\phi(\mathbf{Q})}$) in LES are usually computed using filtered primitive variables ($\tilde{\mathbf{Q}}$) without the consideration of subgrid fluctuations ($\mathbf{Q}''$), that is, $\widetilde{\phi(\mathbf{Q})} = \phi(\tilde{\mathbf{Q}})$. The differ-

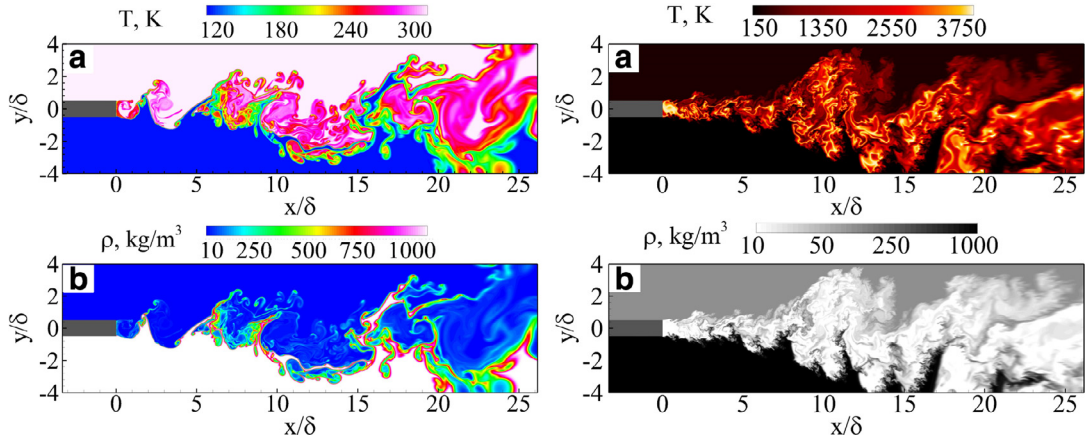

Fig. 4. Instantaneous distributions of temperature and density for cold flow (left) and combustion (right).

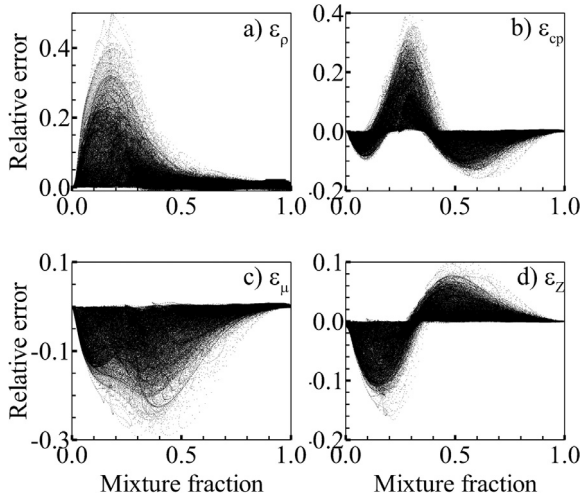

Fig. 5. Relative errors of density, specific heat at constant pressure, dynamic viscosity, and compressibility factor in the mixture fraction space for the cold-flow case.

ence denoted in Eqs. (10)–(14) is evaluated using the present DNS database.

As an example, a LES filter size of 10 ($\bar{\Delta} = 10\Delta$) is applied. Figure 5 shows the relative error ε_ϕ, defined as $\varepsilon_\phi = (\widetilde{\phi(\mathbf{Q})} - \phi(\tilde{\mathbf{Q}}))/\widetilde{\phi(\mathbf{Q})}$, for density, specific heat at constant pressure, dynamic viscosity, and compressibility factor in the mixture fraction space for the cold-flow case. Relative errors of both density and specific heat at constant pressure reach up to 40%, dynamic viscosity up to 20%, and compressibility factor up to 10%. The maximum relative error occurs in the region with the steepest gradient. This can be attributed to insufficient grid resolution and the resulting exclusion of the subgrid effect in LES. These uncertainties are further quantified in the LES equations Eqs. (7)–((9), (18), (19)) through the comparison of SGS terms with filtered terms using the DNS database.

The results show that magnitudes of SGS terms including ρ^{sgs} are comparable to the leading terms in the conservation equations. For example, in the mass equation (Eq. (7)), the RMS of $\partial\rho^{sgs}/\partial t$ is nearly 33% of the temporal term ($\partial\rho(\tilde{\mathbf{Q}})/\partial t$) and 27% of the mass flux term ($\partial(\bar{\rho}\tilde{u}_j)/\partial x_j$). Similarly, the RMS of components of $\partial(\rho^{sgs}\tilde{u}_i)/\partial t$ and $\partial(\rho^{sgs}\tilde{u}_i\tilde{u}_j)/\partial x_j$ take up more than 10% of filtered terms in their respective momentum equations. In the energy equation, the RMS of $\partial(\rho e_t)^{sgs}/\partial t$ is nearly 70% of the filtered temporal term, $\partial(\rho(\tilde{\mathbf{Q}})e_t(\tilde{\mathbf{Q}}))/\partial t$, and the RMS of $\partial((\rho e_t)^{sgs}\tilde{u}_j)/\partial x_j$ is 38% of the filtered energy flux term. The ρ^{sgs}-related terms for the combustion case are also comparable to the leading terms in the governing equations, as discussed in detail in Ref. [44]. This shows the significance of the SGS density for accurate prediction of the filtered density. The uncertainty in the calculated filtered density can propagate forward and contaminate the conservation equations. Reducing the filter size can increase grid resolution and decrease contributions of SGS terms, at the price of increasing computational load. A proper model for ρ^{sgs} in Eq. (15) must be incorporated to reduce the error while maintaining the computational efficiency.

Two strategies are proposed and explored for modeling ρ^{sgs} accounting for the effect of the SGS term in the EOS. The first method is a gradient-based approach, in which the SGS term is modeled as a function of gradients of thermodynamic variables. The second is a mixing-based approach, which includes the effect of subgrid scalar mixing on the thermodynamics.

The gradient-based approach is analogous to the classical eddy-viscosity model. We postulate that the subgrid density has a strong functional relationship with thermodynamic property gradients in the physical space. An obvious example is density gradient, which is a distinctive feature of supercritical flows. Using the DNS database, the correlation between the SGS density term and the gradient of the filtered density is computed. It is found that there is a high correlation factor of about 64–68%, which is comparable to the advanced dynamic and mixed models used for SGS stresses [87]. Motivated by this observation, a model with a functional form similar to that of the Smagorinsky eddy-viscosity model is proposed as

$$\rho^{sgs} = C_1\Delta(|\nabla\tilde{\rho}|) \tag{25}$$

where Δ is the LES filter width and C_1 is a model coefficient determined from the DNS database using a least-square error minimization technique.

SGS terms inherently represent small-scale turbulent mixing processes and their interactions with large-scale resolved motions. Therefore, in addition to including the effects of thermodynamic gradients, it is also essential to model the effects of SGS mixing on the subgrid density. Figure 6a shows the distribution of the subgrid density normalized by the filtered density in the mixture fraction space, where data points are colored with the filtered scalar dissipation rate ($\tilde{\chi}$). The filtered scalar dissipation rate is defined here as:

$$\tilde{\chi} = 2D\widetilde{\left(\frac{\partial f}{\partial x_i}\right)^2} \tag{26}$$

It is seen that subgrid quantities increase with mixture fraction and reach their maxima at the stoichiometric value (0.2), where

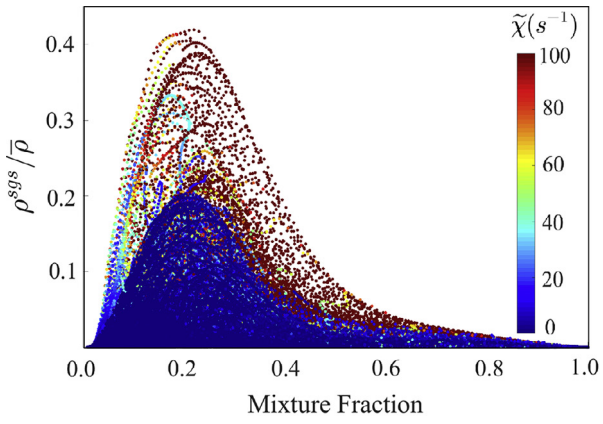

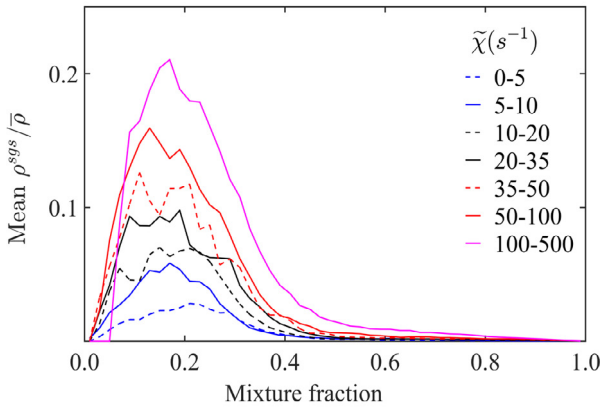

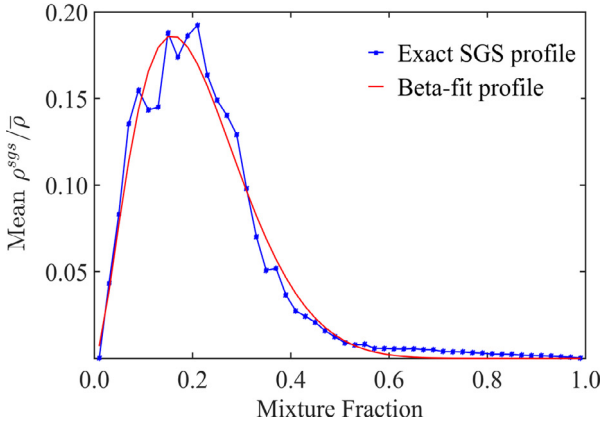

Fig. 6. (a) Distribution of subgrid density normalized by filtered density and colored by filtered scalar dissipation rate in mixture fraction space; (b) profiles of mixture-fraction-conditioned mean of normalized SGS density for a range of scalar dissipation rates (c) example of beta function fit for a profile in the range $\tilde{\chi} = 20 - 35$ s^{-1}. (For interpretation of the references to color in this figure legend, the reader is referred to the web version of this article.)

there is strong mixing between the LOX and methane streams. Regions with a higher filtered scalar dissipation rate have a larger relative error and thus a higher subgrid contribution. This implies that both mixture fraction and scalar dissipation rate are important attributes that characterize the mixing field and can be used to model the SGS term. Taking the mean of the normalized SGS density conditioned on the mixture fraction for a range of filtered scalar dissipation rates, as shown in Fig. 6b, two important trends are noted. First, for each scalar dissipation range, the mean profiles look similar in shape, with a peak close to the stoichiometric mixture fraction. Second, the amplitude of these profiles increases with increase in scalar dissipation rate. Irregularities in the profiles are probably caused by discrete statistical averaging in different mixture fraction bins. Nevertheless, it is found that a best fit for each of these profiles can be approximated by a scaled beta function as

$$\frac{\rho^{sgs}}{\bar{\rho}} \approx C_2 \; beta(f,\ \alpha, \beta) \tag{27}$$

The parameters, $C_2, \alpha,$ and β for the beta function fit are evaluated from the DNS data and listed in Table 1, using a least-squares approximation technique for each filtered scalar dissipation rate range. In agreement with our earlier qualitative findings, it is seen that the shape factors α and β for different ranges are almost the same, while the scaling coefficient C_2 increases with the scalar dissipation rate. Figure 6c shows an example of the beta function fit for the filtered scalar dissipation rate of 20–35 s^{-1}. The norm of the difference between the data profile and the beta function fit for each scalar dissipation rate range is on the order of 0.01.

The two proposed modeling approaches are applied to compute the SGS density to improve the accuracy of the filtered density in Eq. (15). Figure 7 shows the RMS of the relative error conditioned on the mixture fraction for the no-model approach, as compared to the gradient-based and mixing-based models. The RMS error decreases for both approaches, especially in peak errors close to the stoichiometric mixture fraction. The mixing-based approach has stronger and more consistent error reduction in the whole mixture fraction space, while the gradient-based approach produces abnormal error at higher mixture fraction. This over-prediction can be remedied if additional thermodynamic properties gradients, such as temperature, species mass fractions, or higher order gradient terms, are included. Results show that the gradients of temperature and species mass fraction have correlations of nearly 40% and 30%, respectively, with the SGS density [88]. The combined property gradients can reduce the tail error significantly.

Table 1
Coefficients for beta function fit model for each range of scalar dissipation rate.

Range of χ	C	α	β
0–5	0.0081	3.3753	11.9460
5–10	0.0136	3.0000	12.5000
10–20	0.0176	3.1200	12.5000
20–35	0.0222	3.1719	12.8939
35–50	0.0265	3.3194	13.0374
50–100	0.0326	3.0643	11.7768
100–500	0.0414	3.6468	13.0509

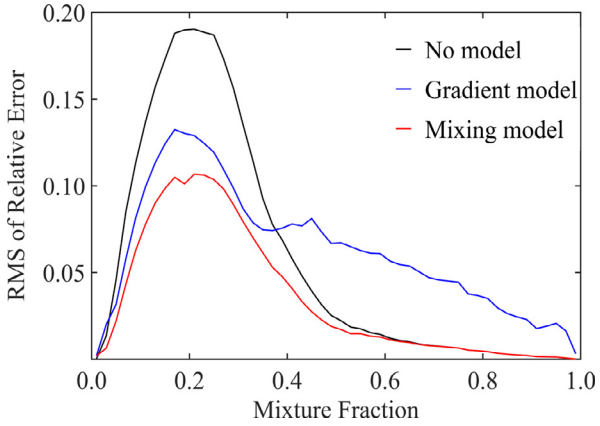

Fig. 7. Comparison of the RMS of relative errors for no model, gradient-based model, and mixing-based model.

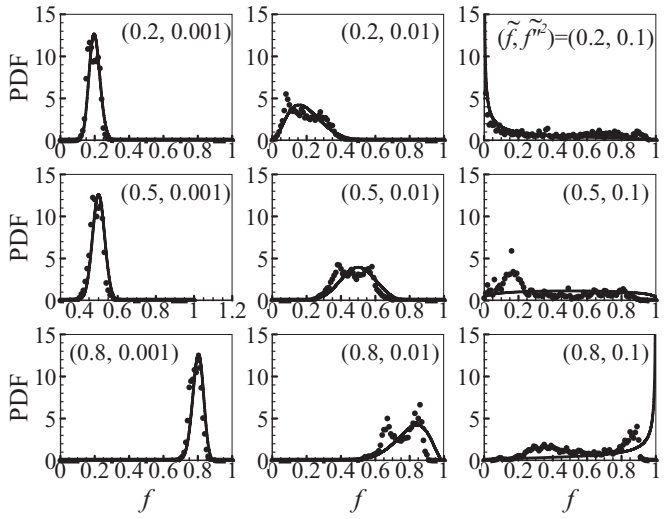

Fig. 8. Comparison of beta-function PDF (solid line) and DNS data-based PDF (symbol) for various means and variances of mixture fraction.

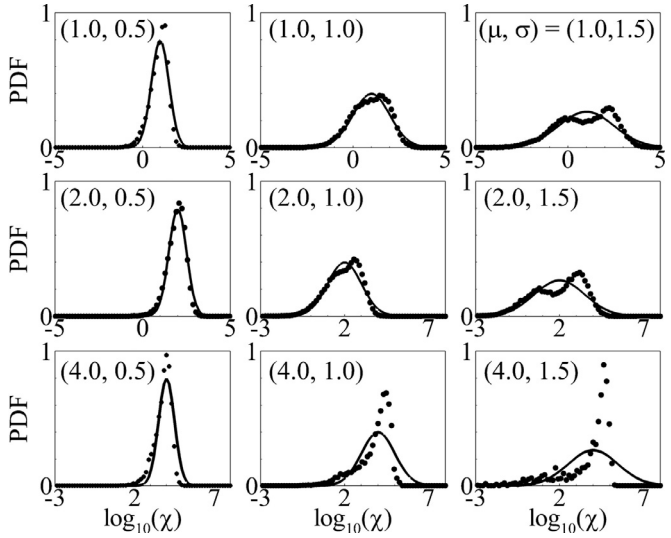

Fig. 9. Comparison of the DNS data-based PDF (symbol) and the lognormal distribution (solid line) of scalar dissipation rate for various means and variances.

4.2. Turbulent combustion modeling

4.2.1. Flamelet-based models

The SLFM and FPV model are incorporated into the coarse-DNS solver as described in Section 4.1. Note that in this context the designation 'coarse-DNS' reflects the ability to resolve all turbulent scales and the technique includes a filtered flamelet approach, in which the filter size is comparable to the flame thickness, to recover chemical reactions at sub-filter scales for reacting flows. This method has been examined for premixed flames [86]. Chemical reactions occur essentially at the smallest scales, and the grid resolution is on the order of the flame thickness. Unresolved flame profiles are retrieved from a pre-calculated flamelet library. For the SLFM, species mass fractions are obtained from solutions of laminar diffusion flames and filtered using the PDFs of mixture fraction and scalar dissipation rate. The former is generally assumed as a beta-function PDF, while the latter is estimated as the lognormal distribution. These two PDFs have previously been validated against DNS results and experimental data only at subcritical conditions, however. Their validity is examined here for supercritical conditions, using the coarse-DNS database.

Figure 8 shows a comparison of the PDFs calculated from the beta function and the DNS database with mean mixture fraction from 0.2 to 0.8 and variance from 0.001 to 0.1. In Fig. 8, the first number in each bracket denotes the mixture fraction and the second is the mixture fraction variance. It is observed that the beta-function distribution can accurately describe the PDF of the DNS data at low variance ($\widetilde{f''^2} = 0.001$), but deviates at higher variance ($\widetilde{f''^2}$=0.01, 0.1). The DNS-extracted PDF is similar to a bimodal distribution with two peaks, one on either side of the mean mixture fraction. The two peaks move away from the mean as the variance increases. Therefore, the beta-function PDF works well only in the region with small mixture fraction variance, and a bimodal function can better represent the PDF at large variance. Figure 9 shows a comparison of the PDF of scalar dissipation rate using the database and the lognormal function at various means and variances. The lognormal distribution can capture the shape of the DNS-extracted PDF, but it underestimates the peak value. The underestimation becomes more prominent at higher mean and variances. Compared to the presumed PDFs, the DNS-extracted PDFs can suitably represent the physical change of flow variables and reduce the filtering error when used to obtain species profiles.

In the FPV model, a transport equation of the progress variable is added to track the global extent of chemical reactions of the local mixture. Filtered species mass fractions and the production rate of the progress variable are obtained by integrating chemical state relationships over a joint subgrid PDF of the mixture fraction and the progress variable. A presumed beta-function PDF is used to describe the subgrid filtered density function of the mixture fraction. Although not shown here, the validity of the beta-function PDF is also limited to a narrow range of mixture fraction variance, as observed from the comparison between the beta-function PDF and the DNS-extracted PDF for the FPV model.

Once a coarse-DNS database is established, the PDFs of the filtered mixture fraction and scalar dissipation rate can be trained and extracted using a data-driven approach. These PDFs can best represent the evolution of the variables in the LES flow field. It could be argued that this approach is problem-dependent, and the data-driven PDFs are only available when a DNS simulation is first performed using the same configuration, making the extra LES simulation redundant. If the shear-layer mixing in the current configurations is treated as a fundamental phenomenon common to all coaxial injectors, however, the DNS-extracted PDF can be utilized to correlate the filtered properties in the turbulent field for other injectors, with flow solutions from the low-dimensional manifold.

4.2.2. Finite-rate chemistry model

In addition to the uncertainty associated with the presumed PDFs, the applicability of flamelet and FPV models also remains controversial, because of the assumptions of scale separation and decoupling between the flamelets and the turbulent flow field. Under high-pressure conditions, where the Reynolds number can be very high, Kolmogorov eddies may penetrate the inner flame structure. To overcome this limitation, multi-species transport equations with detailed finite-rate chemistry are required in the formulation. However, because of the high computational cost, conventional finite-rate LES/DNS typically employs one-step global reaction or over-simplified kinetic mechanisms [43], and this may significantly reduce the quality of prediction. Detailed kinetic mechanisms, on the other hand, are prohibitively computationally expensive, since they contain a large number of species and are numerically stiff and expensive.

To address this issue, an efficient combustion model with finite-rate chemistry, combining DAC and CoTran, has been developed

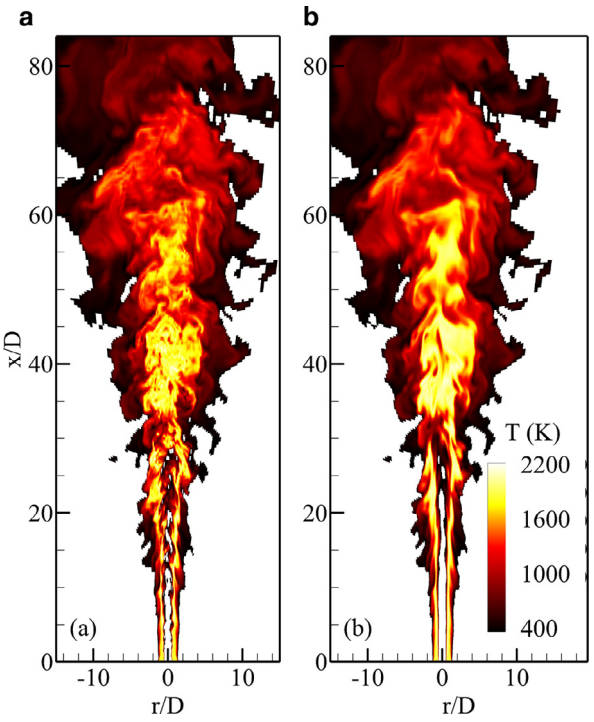

Fig. 10. Snapshots of the temperature field at the same physical time: (a) FPV model and (b) finite-rate chemistry.

and implemented. As an example, a comparative study was conducted on the Sandia Flame D [89], which has an intermediate Reynolds number and a low probability of extinction. Numerical results with the FPV model under the current LES framework have shown excellent agreement with the experimental data in terms of mean and RMS temperature profiles and major species profiles along the centerline [42]. The performance of the finite-rate chemistry/LES is about 6 times faster than the conventional combustion model without DAC and CoTran.

Figure 10 shows distributions of instantaneous temperature at the same physical time using the FPV model and finite-rate chemistry. Although the two methods predict similar time-mean flame structures and flow statistics [71], significant differences are observed in the instantaneous flowfield. The high temperature zone for the finite rate case is wider than that for the FPV case. This may be attributed to the lower CO level for the FPV case, which becomes the rate-controlling factor for the reaction step of the primary heat release reactions: $CO + OH \rightarrow CO_2 + H$. As the Reynolds number increases (Sandia Flames E and F), the probability of local extinction and re-ignition will increase and the advantages of the finite-rate chemistry model will become substantial. This is ongoing research that will be published in subsequent work.

Note that the Sandia Flames were operated at room pressure without real-fluid effects. It will be interesting in the future to incorporate the present efficient finite-rate chemistry model into supercritical flows, which, as mentioned earlier, have high Reynolds numbers induced by high pressure. The finite-rate chemistry effect may be more important. Evaluation of real-fluid thermodynamic and transport properties for those conditions will be challenging, and the computational cost will be much higher than at ideal-gas conditions. Recent studies have found that for non-reacting flows, the computational cost of property evaluation may reach around 50% of the total computation time [61,73]. The next section will introduce two techniques to reduce this cost.

Table 2
Computation time distribution for the baseline, CDE, and tabulation cases.

	Time (ms)	Z (%)	Therm. (%)	Trans. (%)	Others (%)
Baseline	2.97	28.8	19.2	5.5	46.5
CDE	1.77	10.3	9.7	2.3	77.7
Tabulation	1.45	0.1	6.9	2.8	90.2

4.3. Acceleration of real-fluid property evaluation

Tabulation and CDE approaches are examined for a LOX/methane mixing layer at supercritical pressure. The computational setup and operating conditions are identical to those presented in Section 4.1. As the first step of demonstration, the non-reacting case is considered. f (*or* Y_{O_2}) and T are selected as input parameters for tabulation, while T, ρ, *and* Y_{O_2} are chosen as marker variables in the correlation metric for CDE. Previous studies [77–79] have indicated that thermodynamic properties are more sensitive to variations of the marker variables than transport properties. The threshold value is thus set to 0.5% for thermodynamic properties and 2.5% for transport properties. Three parallel cases are computed with identical setup except for evaluation of properties: Case1 – Baseline with on-the-fly property evaluation without special treatment; Case 2 – CDE; Case 3 – Tabulation.

Table 2 lists the time distribution of computing the compressibility factor, thermodynamic properties, transport properties, and other properties. Here 'Time' denotes the average time taken to perform calculation for one iteration. Compared to the baseline case, a remarkable acceleration is achieved in property evaluation through both the CDE and tabulation approaches. The CDE approach reduces the evaluation time for the compressibility factor by 4.8 times, thermodynamic properties by 3.3 times, and transport properties by 4.2 times. This leads to a significant drop in percentage of computation time devoted to property evaluation ($\sim$ 22.3% vs 53.5% for the baseline) and consequently a 40.4% saving in total time. The performance of the tabulation approach is even better, with less than 10% used in property calculations and more than 50% saving in total time.

The prediction accuracy of the two methods is also examined. Figure 11 shows a comparison of the distributions of compressibility factor and dynamic viscosity at the same physical time for the three cases. Both CDE and tabulation methods show good agreement with the baseline, with the CDE method in particular accurately capturing the fine structures in the mixing layer. However, the tabulation method does not predict the fine structures in the circled wake and downstream regions. The discrepancy in the dynamic viscosity may change the values of the actual viscous stress in the shear layer and thus induce different small structures in the wake region. A more obvious discrepancy occurs near the exit; the compressibility factor is lower and the dynamic viscosity is slightly higher. This might be related to the combined effects of the tabulation interpolation and the outlet boundary conditions. The pressure outlet condition may result in uncertainties in the fluctuating flowfield, which can contaminate the evaluation of other properties. In future work, the pressure effect and more gradient-adaptive interpolation will be included to reduce uncertainty.

The CDE approach seems to be promising in terms of accuracy and efficiency. For the combustion case, the performance will be superior, since more species will be involved. The efficient property evaluation scheme can be incorporated into the framework introduced in Section 5 with the finite-rate chemistry in LES to further speed up the simulation of supercritical combustion. The combined framework is expected to explore more salient features, such as unsteady events, that the existing numerical scheme and experiments cannot capture.

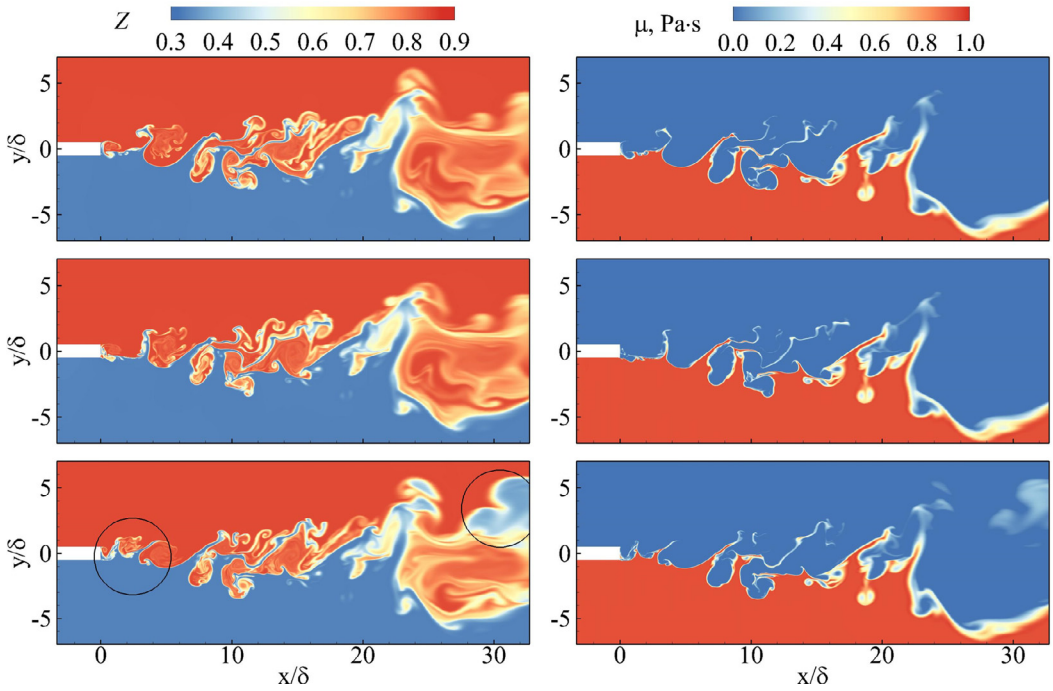

Fig. 11. Comparison of calculated compressibility factor (left) and dynamic viscosity (right) using the baseline (upper), CDE (middle), and tabulation (lower) cases.

5. Conclusions

This paper presents systematic efforts to address the challenges of modeling and simulation of supercritical fluid mixing and combustion. The LES-based theoretical framework is described with new density-related subgrid terms. Although the previously available framework is capable of exploring many problems related to supercritical fluids, the present paper offers the possibility of more accurate and computationally efficient modeling and simulation by addressing several critical issues, including unclosed SGS modeling, presumed PDFs for combustion modeling, and evaluation of detailed chemistry and real-fluid properties.

In calculations of filtered thermodynamic properties, the SGS contributions of filtered primitive variables, usually neglected for ideal gases, were evaluated for real fluids using a DNS database for a LOX/methane supercritical mixing layer. The relative error of the filtered density was found to be up to 40%. This uncertainty propagates forward and contaminates calculations of the conservation equations, in which SGS density-related terms become comparable to the leading-order terms. Two closure models were proposed for the SGS density in EOS: a gradient-based and a mixing-based approach. Both approaches were found to considerably reduce the modeling error.

Flamelet-based models with presumed PDFs were investigated for applications at supercritical conditions. The DNS-extracted PDFs of mixture fraction and scalar dissipation rate were compared with the corresponding presumed PDFs using a data-driven approach. The PDF of the mixture fraction shows good agreement with the beta-function distribution only at small mixture fraction variance (< 0.01). The shape of the PDF of scalar dissipation rate is similar to the lognormal distribution but has a larger amplitude. The current DNS-extracted PDFs may be implemented to more general configurations with shear-layer-dominated flow structures.

An alternative combustion model with finite-rate chemistry was also explored. Direct incorporation of detailed finite-rate chemistry into the LES framework is computationally prohibitive. To circumvent this challenge, the model incorporates dynamic adaptive chemistry and correlated transport, and is numerically treated using a point-implicit ODE solver. It was validated against the Sandia Flame D at atmospheric pressure. Significant improvement of computational efficiency was achieved. This efficient finite-rate chemistry model will be implemented for the supercritical regime in the future.

Finally, the computational efficiency of real-fluid property evaluation was considerably enhanced by means of the tabulation and correlated dynamic evaluation approaches. The latter achieved better overall accuracy. Efficient chemistry calculation, correlated dynamic evaluation of real-fluid properties, and the proposed SGS density models can be used to establish a unified LES/finite-rate chemistry framework for modeling supercritical fluid flows and combustion more accurately and efficiently.

Acknowledgments

This work was sponsored partly by the Air Force Office of Scientific Research under Grant no. FA 9550-10-1-0179, and partly by the William R. T. Oakes Endowment of the Georgia Institute of Technology. The authors gratefully acknowledge support and advice from Mitat A. Birkan.

References

[1] V. Yang, Modeling of supercritical vaporization, mixing, and combustion processes in liquid-fueled propulsion systems, Proc. Combust. Inst. 28 (2000) 925–942.
[2] J. Bellan, Supercritical (and subcritical) fluid behavior and modeling: drops, streams, shear and mixing layers, jets and sprays, Prog. Energy Combust. Sci. 26 (2000) 329–366.
[3] M. Oschwald, J.J. Smith, R. Branam, J. Hussong, A. Schik, B. Chehroudi, D. Talley, Injection of fluids into supercritical environments, Combust. Sci. Technol. 178 (2006) 49–100.
[4] R.N. Dahms, J.C. Oefelein, On the transition between two-phase and single-phase interface dynamics in multicomponent fluids at supercritical pressures, Phys. Fluids 25 (2013) 092103.
[5] W.O.H. Mayer, H. Tamura, Propellant injection in a liquid oxygen/gaseous hydrogen rocket engine, J. Propuls. Power 12 (1996) 1137–1147.
[6] W.O.H. Mayer, A.H.A. Schik, B. Vielle, C. Chauveau, I. Gokalp, D.G. Talley, R.D. Woodward, Atomization and breakup of cryogenic propellants under high-pressure subcritical and supercritical conditions, J. Propuls. Power 14 (1998) 835–842.

[7] B. Chehroudi, D. Talley, E. Coy, Visual characteristics and initial growth rates of round cryogenic jets at subcritical and supercritical pressures, Phys. Fluids 14 (2002) 850–861.
[8] V. Yang, M. Habiballah, J. Hulka, M. Popp, Liquid rocket thrust chambers: aspects of modeling, analysis, and design, Progress in Astronautics and Aeronautics, AIAA (2004), p. 200.
[9] G. Singla, P. Scouflaire, C. Rolon, S. Candel, Transcritical oxygen/transcritical or supercritical methane combustion, Proc. Combust. Inst. 30 (2005) 2921–2928.
[10] S. Candel, M. Juniper, G. Singla, P. Scouflaire, C. Rolon, Structure and dynamics of cryogenic flames at supercritical pressure, Combust. Sci. Technol. 178 (2006) 161–192.
[11] T. Schmitt, J. Rodriguez, I. Leyva, S. Candel, Experiments and numerical simulation of mixing under supercritical conditions, Phys. Fluids 24 (2012) 055104.
[12] A. Roy, C. Segal, Experimental study of fluid jet mixing at supercritical conditions, J. Propuls. Power 26 (2010) 1205–1211.
[13] S. DeSouza, C. Segal, Sub-and supercritical jet disintegration, Phys. Fluids 29 (2017) 047107.
[14] J.C. Oefelein, V. Yang, Modeling high-pressure mixing and combustion processes in liquid rocket engines, J. Propuls. Power 14 (1998) 843–857.
[15] N.A. Okong'o, J. Bellan, Direct numerical simulation of a transitional supercritical binary mixing layer: heptane and nitrogen, J. Fluid Mech. 464 (2002) 1–34.
[16] N. Zong, H. Meng, S.-Y. Hsieh, V. Yang, A numerical study of cryogenic fluid injection and mixing under supercritical conditions, Phys. Fluids 16 (2004) 4248–4261.
[17] J.C. Oefelein, Thermophysical characteristics of shear-coaxial LOX–H_2 flames at supercritical pressure, Proc. Combust. Inst. 30 (2005) 2929–2937.
[18] M. Masquelet, S. Menon, Large-eddy simulation of flame-turbulence interactions in a shear coaxial injector, J. Propuls. Power 26 (2010) 924–935.
[19] T. Schmitt, Y. Méry, M. Boileau, S. Candel, Large-eddy simulation of oxygen/methane flames under transcritical conditions, Proc. Combust. Inst. 33 (2011) 1383–1390.
[20] P.C. Ma, Y. Lv, M. Ihme, An entropy-stable hybrid scheme for simulations of transcritical real-fluid flows, J. Comput. Phys. 340 (2017) 330–357.
[21] H. Müller, C.A. Niedermeier, J. Matheis, M. Pfitzner, S. Hickel, Large-eddy simulation of nitrogen injection at trans-and supercritical conditions, Phys. Fluids 28 (2016) 015102.
[22] P. Tucker, S. Menon, C. Merkle, J. Oefelein, V. Yang, Validation of high-fidelity CFD simulations for rocket injector design, 44th AIAA/ASME/SAE/ASEE Joint Propulsion Conference (2008), pp. 2008–5226.
[23] H. Müller, J. Zips, M. Pfitzner, D. Maestro, B. Cuenot, L. Selle, R. Ranjan, P. Tudisco, S. Menon, Numerical investigation of flow and combustion in a single-element GCH_4/GOX rocket combustor: a comparative LES study, 52nd AIAA/SAE/ASEE Joint Propulsion Conference (2016), pp. 2016–4997.
[24] A.M. Ruiz, G. Lacaze, J.C. Oefelein, R. Mari, B. Cuenot, L. Selle, T. Poinsot, Numerical benchmark for high-Reynolds-number supercritical flows with large density gradients, AIAA J. 54 (2015) 1445–1460.
[25] D.T. Banuti, Crossing the widom-line – supercritical pseudo-boiling, J. Supercrit. Fluids 98 (2015) 12–16.
[26] S. Karni, Hybrid multifluid algorithms, SIAM J. Sci. Comput. 17 (1996) 1019–1039.
[27] X. Wang, H. Huo, Y. Wang, V. Yang, Comprehensive study of cryogenic fluid dynamics of swirl injectors at supercritical conditions, AIAA J. 55 (2017) 3109–3119.
[28] H. Terashima, M. Koshi, Approach for simulating gas–liquid-like flows under supercritical pressures using a high-order central differencing scheme, J. Comput. Phys. 231 (2012) 6907–6923.
[29] S.-Y. Hsieh, V. Yang, A preconditioned flux-differencing scheme for chemically reacting flows at all Mach numbers, Int. J. Comput. Fluid Dyn. 8 (1997) 31–49.
[30] N. Zong, V. Yang, An efficient preconditioning scheme for real-fluid mixtures using primitive pressure–temperature variables, Int. J. Comput. Fluid Dyn. 21 (2007) 217–230.
[31] P.C. Le Clercq, J. Bellan, Modeling of multicomponent-fuel drop-laden mixing layers having a multitude of species, Proc. Combust. Inst. 30 (2005) 2011–2019.
[32] J. Bellan, Theory, modeling and analysis of turbulent supercritical mixing, Combust. Sci. Technol. 178 (2006) 253–281.
[33] P.E. Lapenna, F. Creta, Mixing under transcritical conditions: an a-priori study using direct numerical simulation, J. Supercrit. Fluids 128 (2017) 263–278.
[34] J. Bellan, Direct numerical simulation of a high-pressure turbulent reacting temporal mixing layer, Combust. Flame 176 (2017) 245–262.
[35] J. Bellan, Evaluation of mixture-fraction-based turbulent-reaction-rate model assumptions for high-pressure reactive flows, Combust. Flame 179 (2017) 253–266.
[36] J.C. Oefelein, Large eddy simulation of turbulent combustion processes in propulsion and power systems, Prog. Aerosp. Sci 42 (2006) 2–37.
[37] N. Zong, V. Yang, Cryogenic fluid jets and mixing layers in transcritical and supercritical environments, Combust. Sci. Technol. 178 (2006) 193–227.
[38] X. Petit, G. Ribert, G. Lartigue, P. Domingo, Large-eddy simulation of supercritical fluid injection, J. Supercrit. Fluids 84 (2013) 61–73.
[39] G. Ribert, D. Taieb, V. Yang, Large-eddy simulation of a supercritical channel flow using a shock capturing numerical scheme, Comput. Fluids 117 (2015) 103–113.
[40] H. Müller, M. Pfitzner, J. Matheis, S. Hickel, Large-eddy simulation of coaxial LN2/GH2 injection at trans-and supercritical conditions, J. Propuls. Power 32 (2015) 46–56.
[41] X. Wang, V. Yang, Supercritical mixing and combustion of liquid-oxygen/kerosene bi-swirl injectors, J. Propuls. Power 33 (2016) 316–322.
[42] H. Huo, V. Yang, Large-eddy simulation of supercritical combustion: model validation against gaseous H_2–O_2 injector, J. Propul. Power 33 (2017) 1272–1284.
[43] L.C. Selle, N.A. Okong'o, J. Bellan, K.G. Harstad, Modelling of subgrid-scale phenomena in supercritical transitional mixing layers: an a priori study, J. Fluid Mech. 593 (2007) 57–91.
[44] H. Huo, V. Yang, Subgrid-scale models for large-eddy simulation of supercritical combustion, 51st AIAA Aerospace Sciences Meeting (2013) pp. 2013–706.
[45] G. Ribert, X. Petit, P. Domingo, High-pressure methane-oxygen flames. Analysis of sub-grid scale contributions in filtered equations of state, J. Supercrit. Fluids 121 (2017) 78–88.
[46] N. Peters, Laminar diffusion flamelet models in non-premixed turbulent combustion, Prog. Energy Combust. Sci. 10 (1984) 319–339.
[47] A.W. Cook, J.J. Riley, G. Kosály, A laminar flamelet approach to subgrid-scale chemistry in turbulent flows, Combust. Flame 109 (1997) 332–341.
[48] C.D. Pierce, P. Moin, Progress-variable approach for large-eddy simulation of non-premixed turbulent combustion, J. Fluid Mech. 504 (2004) 73–97.
[49] H. Pitsch, Large-eddy simulation of turbulent combustion, Annu. Rev. Fluid Mech. 38 (2005) 453–482.
[50] A.Y. Klimenko, R.W. Bilger, Conditional moment closure for turbulent combustion, Prog. Energy Combust. Sci. 25 (1999) 595–687.
[51] I.S. ErtesvÅG, B.F. Magnussen, The eddy dissipation turbulence energy cascade model, Combust. Sci. Technol. 159 (2000) 213–235.
[52] O. Colin, F. Ducros, D. Veynante, T. Poinsot, A thickened flame model for large eddy simulations of turbulent premixed combustion, Phys. Fluids 12 (2000) 1843–1863.
[53] S. Menon, A.R. Kerstein, The linear-eddy model, turbulent combustion modeling: advances, new trends and perspectives, Springer Netherlands, Dordrecht (2011), pp. 221–247.
[54] S.B. Pope, PDF methods for turbulent reactive flows, Prog. Energy Combust. Sci. 11 (1985) 119–192.
[55] J.C. Oefelein, Analysis of turbulent combustion modeling approaches for aero-propulsion applications, 53rd AIAA Aerospace Sciences Meeting, 2015 2015-1378.
[56] R.S. Miller, J.W. Foster, Survey of turbulent combustion models for large-eddy simulations of propulsive flowfields, AIAA J. 54 (2016) 2930–2946.
[57] E.D. Gonzalez-Juez, A.R. Kerstein, R. Ranjan, S. Menon, Advances and challenges in modeling high-speed turbulent combustion in propulsion systems, Prog. Energy Combust. Sci. 60 (2017) 26–67.
[58] A.W. Cook, J.J. Riley, A subgrid model for equilibrium chemistry in turbulent flows, Phys. Fluids 6 (1994) 2868–2870.
[59] C. Wall, B.J. Boersma, P. Moin, An evaluation of the assumed beta probability density function subgrid-scale model for large eddy simulation of non-premixed, turbulent combustion with heat release, Phys. Fluids 12 (2000) 2522–2529.
[60] D. Huang, Q. Wang, H. Meng, Modeling of supercritical-pressure turbulent combustion of hydrocarbon fuels using a modified flamelet-progress-variable approach, Appl. Therm. Eng. 119 (2017) 472–480.
[61] K.C. Gottiparthi, R. Sankaran, A.M. Ruiz, G. Lacaze, J.C. Oefelein, Large eddy simulation of a supercritical fuel jet-in-cross-flow using GPU acceleration, 54th AIAA Aerospace Sciences Meeting, 2016 2016-1939.
[62] G. Lacaze, J.C. Oefelein, A non-premixed combustion model based on flame structure analysis at supercritical pressures, Combust. Flame 159 (2012) 2087–2103.
[63] X. Petit, G. Ribert, P. Domingo, Framework for real-gas compressible reacting flows with tabulated thermochemistry, J. Supercrit. Fluids 101 (2015) 1–16.
[64] B.E. Poling, J.M. Prausnitz, J.P. O'connell, The properties of gases and liquids, Mcgraw-hill, New York, 2001.
[65] M.S. Graboski, T.E. Daubert, A modified Soave equation of state for phase equilibrium calculations. 1. Hydrocarbon systems, Ind. Eng. Chem. Process Des. Dev. 17 (1978) 443–448.
[66] S.B. Pope, Turbulent flows, IOP Publishing, 2001.
[67] P.E. DesJardin, S.H. Frankel, Large eddy simulation of a nonpremixed reacting jet: application and assessment of subgrid-scale combustion models, Phys. Fluids 10 (1998) 2298–2314.
[68] W. Sun, Z. Chen, X. Gou, Y. Ju, A path flux analysis method for the reduction of detailed chemical kinetic mechanisms, Combust. Flame 157 (2010) 1298–1307.
[69] S. Yang, R. Ranjan, V. Yang, S. Menon, W. Sun, Parallel on-the-fly adaptive kinetics in direct numerical simulation of turbulent premixed flame, Proc. Combust. Inst. 36 (2017) 2025–2032.
[70] S. Yang, R. Ranjan, V. Yang, W. Sun, S. Menon, Sensitivity of predictions to chemical kinetics models in a temporally evolving turbulent non-premixed flame, Combust. Flame 183 (2017) 224–241.
[71] S. Yang, X. Wang, V. Yang, W. Sun, H. Huo, Comparison of flamelet/progress-variable and finite-rate chemistry LES models in a preconditioning scheme, 55th AIAA Aerospace Sciences Meeting, 2017 2017-0605.
[72] H. Meng, V. Yang, A unified treatment of general fluid thermodynamics and its application to a preconditioning scheme, J. Comput. Phys. 189 (2003) 277–304.
[73] S. Yang, Y. Li, X. Wang, U. Unnikrishnan, V. Yang, W. Sun, Comparison of tabulation and correlated dynamic evaluation of real fluid properties for supercritical mixing, 53rd AIAA/SAE/ASEE Joint Propulsion Conference (2017), pp. 2017–4858.
[74] R.C. Swanson, E. Turkel, On central-difference and upwind schemes, J. Comput. Phys. 101 (1992) 292–306.

[75] H. Meng, G. Hsiao, V. Yang, J. Shuen, Transport and dynamics of liquid oxygen droplets in supercritical hydrogen streams, J. Fluid Mech. 527 (2005) 115–139.
[76] G.C. Hsiao, H. Meng, V. Yang, Pressure-coupled vaporization response of n-pentane fuel droplet at subcritical and supercritical conditions, Proc. Combust. Inst. 33 (2011) 1997–2003.
[77] G. Ribert, N. Zong, V. Yang, L. Pons, N. Darabiha, S. Candel, Counterflow diffusion flames of general fluids: oxygen/hydrogen mixtures, Combust. Flame 154 (2008) 319–330.
[78] H. Huo, X. Wang, V. Yang, A general study of counterflow diffusion flames at subcritical and supercritical conditions: oxygen/hydrogen mixtures, Combust. Flame 161 (2014) 3040–3050.
[79] X. Wang, H. Huo, V. Yang, Counterflow diffusion flames of oxygen and n-alkane hydrocarbons (CH_4-$C_{16}H_{34}$) at subcritical and supercritical conditions, Combust. Sci. Technol. 187 (2014) 60–82.
[80] N. Zong, V. Yang, Near-field flow and flame dynamics of LOX/methane shear–coaxial injector under supercritical conditions, Proc. Combust. Inst. 31 (2007) 2309–2317.
[81] N. Zong, V. Yang, Cryogenic fluid dynamics of pressure swirl injectors at supercritical conditions, Phys. Fluids 20 (2008) 056103.
[82] X. Wang, Y. Wang, V. Yang, Geometric effects on liquid oxygen/kerosene bi-swirl injector flow dynamics at supercritical conditions, AIAA J. 55 (2017) 3467–3475.
[83] A.A. Vasin, S.D. Kamensky, B.I. Katorgin, A.I. Kolesnikov, V.P. Nosov, A.I. Stavrulov, V.V. Fedorov, V.K. Chvanov, Liquid-propellant rocket engine chamber and its casing, US Patents, 2001.
[84] M.L. Dranovsky, V. Yang, F. Culick, D.G. Talley, Combustion instabilities in liquid rocket engines: testing and development practices in Russia, Progress in Astronautics and Aeronautics, AIAA (2007), p. 221.
[85] Q.-D. Wang, Y.-M. Fang, F. Wang, X.-Y. Li, Skeletal mechanism generation for high-temperature oxidation of kerosene surrogates, Combust. Flame 159 (2012) 91–102.
[86] S. Mukhopadhyay, R. Bastiaans, J. van Oijen, L. de Goey, Analysis of a filtered flamelet approach for coarse DNS of premixed turbulent combustion, Fuel 144 (2015) 388–399.
[87] M.P. Martin, U. Piomelli, G.V. Candler, Subgrid-scale models for compressible large-eddy simulations, Theor. Comput. Fluid Dyn. 13 (2000) 361–376.
[88] U. Unnikrishnan, X. Wang, S. Yang, V. Yang, Subgrid scale modeling of the equation of state for turbulent flows under supercritical conditions, 53rd AIAA/SAE/ASEE Joint Propulsion Conference (2017), pp. 2017–4855.
[89] R.S. Barlow, J.H. Frank, Effects of turbulence on species mass fractions in methane/air jet flames, Symp. (Int.) Combust. 27 (1998) 1087–1095.